Nonlinear Propagation of Supersonic Fan Tones in Turbofan Intake Ducts

Oluwaseun E. Adetifa[a], Alan McAlpine[b] and Gwénaël Gabard[c]
University of Southampton, Southampton, SO17 1BJ United Kingdom

Supersonic fan tones are a critical issue for large fans; it is well known that these tones are a key noise source at high power operating conditions for modern turbofan aero-engines. Nonlinear propagation of the rotor-locked pressure field generated in a turbofan intake duct is calculated by implementing nonlinear weak-shock theory numerically via a combined time-frequency domain algorithm. The aim of the prediction method is to model the nonlinear attenuation and liner absorption of the rotor-locked pressure field within the intake duct. In this hybrid method, the time-domain approach provides a robust and accurate prediction of the non-linear attenuation while the frequency domain is required to represent the liner attenuation. The focus of this work is to compare the time-frequency domain method with time-domain or frequency-domain methods which have been developed previously to calculate the nonlinear propagation of the rotor-locked pressure field in either a rigid or lined intake duct respectively. The capability of the time-frequency domain method to calculate accurately the nonlinear propagation of the rotor-locked pressure field, which can provide an engineering method for buzz-saw noise prediction, is demonstrated.

[a] Research Fellow, Institute of Sound and Vibration Research, University of Southampton, Southampton, SO17 1BJ UK.

[b] Associate Professor, Institute of Sound and Vibration Research, University of Southampton, Southampton, SO17 1BJ UK.

[c] Present contact details: Researcher, LAUM, Université du Maine, 72000 Le Mans, France. AIAA Senior Member. gwenael.gabard@univ-lemans.fr

Nomenclature

B	= number of fan blades
BPF	= blade passing frequency
c, c_0	= local speed of sound, reference speed of sound
D	= duct diameter
EO	= $f/\mathcal{F}$, engine order
f	= frequency
$\mathcal{F}$	= engine's shaft rotation frequency
h	= cavity depth
i	= $\sqrt{-1}$
J_m	= Bessel function of the first kind, order m
k	= ω/c_0, wavenumber
k_z	= axial wavenumber
K	= parameter linking T and z, $T = (z/D)K$
M_a, M_t, M_{rel}	= axial, fan tip, relative Mach number
m, n	= azimuthal order, radial order
N	= number of grid points
p, p_0	= fluid pressure, reference (mean) pressure
p'	= $p - p_0$, acoustic pressure (deviation from p_0)
P	= non-dimensional acoustic pressure
p'_e	= pressure at point on expansion wave (deviation from p_0)
p'_{sm}	= shock mid-point pressure (deviation from p_0)
r, θ, z	= components of the cylindrical polar coordinate system
R	= non-dimensional specific acoustic resistance
s	= $\Delta p_s(0)/p_0$, non-dimensional initial shock strength
t	= time
T	= non-dimensional time of flight

u = fluid velocity

v_e, v_s = velocity at point on expansion wave, velocity of shock

x = propagation distance of the one-dimensional sawtooth waveform

$\bar{x}$ = propagation distance in moving reference frame, $x - c_0 t$

X or Y = non-dimensional propagation distance in moving reference frame

X_m, X_c = non-dimensional specific acoustic mass reactance, cavity reactance

Z = non-dimensional specific acoustic impedance

β = $(\gamma + 1)/2$

γ = ratio of specific heats

Δp_s = shock amplitude

ε = dissipation constant

κ = radial eigenvalue

λ = shock-spacing for regular sawtooth

ρ = fluid density

$\sigma(m)$ = liner absorption rate, azimuthal order m

σ_B = liner absorption rate at BPF

ω = angular frequency

Subscripts

0 = reference value

e = expansion wave

s = shock wave

mn = mode (m, n)

r = real part

i = imaginary part

j = jth grid point

Superscripts

$'$ = acoustic perturbation

$\hat{}$ = time-harmonic perturbation

n = time step index

$\bar{}$ = average value

I. Introduction

Advanced modelling techniques to improve understanding of the generation and propagation of noise from aircraft are necessary to aid the ongoing technological developments by aircraft manufacturers to reduce perceived aircraft noise levels. Reliable models that can predict the levels of the radiated sound from a range of different sources of aircraft noise are required in order to ensure that increasingly stringent civil aviation noise regulations can be met [1, 2].

The shift from single-core jet engines to high-bypass-ratio turbofan engines brought about a reduction in the overall aircraft engine noise, predominantly by reducing the jet broadband noise. The evolution of turbofan engines has led to large-diameter ducted fans. Thus, in modern high-bypass-ratio turbofan engines, the fan is a major contributor to the overall aircraft noise levels at high engine power settings such as during aircraft take off [2].

At high-power settings, the relative speed between the rotating fan and the approaching flow becomes supersonic and shock waves are generated at the fan blade tips. The field comprised of these shocks is referred to as the "rotor-locked" pressure field because the pattern of shock waves, which originates at the fan plane, propagates upstream through the incoming flow in a helical path, spinning with the same angular velocity as the fan's rotor blades [3, 4]. The rotor-locked pressure field comprised of the shock waves formed at the fan blade tips is composed of harmonics of the engine shaft rotation frequency, known as the engine order (EO) harmonics [1, 2]. The noise produced by this mechanism at supersonic relative fan-tip speeds is mainly tonal, and is referred to colloquially as "buzz-saw" noise, or alternatively also as "multiple-pure" tones or "combination" tones.

Since supersonic fan tones are a prevalent issue connected to modern high-bypass-ratio turbofan engines, practical engineering methods capable of accurate prediction of supersonic fan tones are a key requirement associated with the prediction and control of aircraft noise. In this article, existing time- or frequency-domain engineering prediction methods for supersonic fan tones are briefly reviewed. These methods are used to benchmark a new method based on a hybrid time-frequency domain algorithm for one-dimensional nonlinear waves [5]. This category of numerical schemes for nonlinear acoustics is described in the text by Hamilton and Blackstock ([6], Chapter 11,

pp. 319–324). The focus of this work is the development of such a time-frequency domain method to predict the nonlinear propagation and liner absorption of the rotor-locked pressure field within a turbofan intake duct. In this hybrid method the time-domain approach provides a robust and accurate prediction of the non-linear attenuation while the frequency domain is required to represent the liner attenuation. The hybrid method therefore combines the strength of both approaches. This model represents the central building block in an on-going effort towards a prediction method for weak shock propagation in axisymmetric ducts with axially-varying geometry, flow and liner attenuation which will be fast and reliable for engineering predictions of supersonic fan tones.

This is the first article where a time-frequency domain method for application to the prediction of supersonic fan tones is outlined in full, and benchmarked against separate time-domain or frequency-domain methods which have been developed previously for application to the same problem. It is noted that results obtained with a similar approach were presented by Kassem [7], but there was no explicit description given of the numerical schemes or the formulation of the model for nonlinear propagation. For benchmarking purposes, the time-domain method is applicable for simulations of the nonlinear propagation in a rigid intake, whereas the frequency-domain method was developed primarily for simulations of the nonlinear propagation in a lined intake. Also selected validation results are shown of comparisons between computational predictions and experimental measurements of supersonic fan tones obtained from a model-scale fan rig test.

In the design and optimisation of engineering systems, fast and efficient methods for evaluating the effects of changes to various parameters are desirable as this will enable different configurations to be assessed quickly. The propagation of the rotor-locked pressure field for a supersonic ducted fan is known to be sensitive to small parametric changes, notably small blade-to-blade differences, which can significantly affect the noise levels of this source. Elaborate computational fluid dynamics (CFD) models (such as that used for nonlinear propagation in reference [8]) are very expensive and are not feasible, at present, to use for parametric studies associated with the prediction of supersonic fan tones, owing to the high computational costs involved. Hence, the work reported in this article was carried out to develop a method which can predict the propagation of the rotor-locked pressure field to a high-degree of reliability, providing accurate results efficiently without recourse to large-

scale CFD computations, but capturing all the key physical mechanisms involved in the nonlinear propagation process.

A one-dimensional sawtooth pressure waveform is used to represent the rotor-locked field generated by a supersonic ducted fan. This approach was first developed in detail by Morfey and Fisher [3], which made significant progress from earlier investigations into the propagation of high-amplitude sound waves in uniform cylindrical waveguides [9, 10]. Following the work by Morfey and Fisher, McAlpine and Fisher [4, 11] extended their approach to model an irregular sawtooth waveform which accounts for small blade-to-blade variations, and can be used directly to predict buzz-saw noise. This approach considers the shock waves formed at the fan blade tips, but neglects the radial distribution of the shocks over the blades' span. This assumption is valid provided that the region of supersonic flow is largely confined to the region near the fan blade tips, whence the pressure around the duct's circumference can be modelled by a one-dimensional waveform. Propagation of this rotor-locked pressure field is nonlinear owing to the presence of shock waves and consequently the pressure amplitudes inside the intake duct are not at linear levels.

It has been shown that this type of model can capture the main features of this pressure field [12–14], and propagation of input one-dimensional waveforms generated from measurements close to the fan [11, 15] or by means of blade stagger angles values [16] show the reliability of the one-dimensional approximation of the pressure field. Prasad [17] compared the results based on such an approximation against three-dimensional numerical simulations and assessed the effect of the radial span of the pressure field.

Modified weak-shock theory [18] is the basis of the nonlinear propagation model. A hybrid algorithm is used to implement weak-shock theory [3, 4, 11, 19] to model the nonlinear propagation in the time domain, combined with linear duct acoustics theory to model absorption by an acoustic liner in the frequency domain. The progressive distortion and attenuation of the waveform as it propagates upstream in the intake duct can be captured at any specified axial station.

Section II presents the one-dimensional theoretical model for the propagation of weak shocks. Existing methods used to solve this model in the time or the frequency domains are then reviewed. This is necessary since the proposed hybrid method, presented in Section III, is a combination

of these two approaches. Section III also provides details of the numerical implementation of the method. In Section IV, the method is verified and compared against existing time-domain results, frequency-domain results, and, also, examples of measured data. The main findings are summarised in Section V and future extensions of the method are outlined.

II. Supersonic fan tones and nonlinear propagation models

A major component of the noise at high-power engine operating conditions is the supersonic fan tones which we refer to also as buzz-saw noise. Shocks are produced at the fan blade tips. The shocks propagate upstream, against the inflow, following a helical path locked to the rotation of the fan [4, 11]. The pressure field around the duct's circumference, produced at the fan blade tips, can be modelled as a series of shock waves and expansion waves, which form a sawtooth pressure waveform.

Blade-to-blade variations are the cause of small differences between the shocks in the sawtooth. The shocks propagate at speeds which depend on each shock's mid-point pressure (average of the shock's maximum and minimum pressure). Therefore the shocks in an irregular sawtooth propagate at different speeds relative to each other. Whilst the sawtooth waveform propagates against the incoming flow, the shocks are attenuated via nonlinear decay, also faster shocks catch up with slower ones and the shocks can merge. Additionally, an acoustic liner installed on the intake duct wall can attenuate the rotor-locked pressure field, thus absorbing sound energy.

The relative difference in speeds of the shocks, and the interactions among the shocks, lead to a transfer of energy among the EO harmonics. These nonlinear interactions can shift the dominance from the blade passing frequency (BPF) and its harmonics, notably to low-order EO harmonics at frequencies less than BPF. This can result in the low-frequency, ragged buzz-saw noise perceived by observers in the far field, once the rotor-locked pressure field has been radiated from the duct.

A. Nonlinear propagation for one-dimensional acoustic waves

The rotor-locked pressure field is represented, approximately, by a one-dimensional sawtooth waveform with propagation direction denoted by x, which traces a helical path inside a cylindrical intake duct. Assuming that the shocks are weak, the change in entropy across the shocks is negligible,

and the energy equation can be replaced by the equation of state for an isentropic perfect gas. Accordingly, the one-dimensional equations of continuity, momentum and state can be expressed as

$$\left(\frac{\partial}{\partial t} + u\,\frac{\partial}{\partial x}\right)\rho + \rho\,\frac{\partial u}{\partial x} = 0\,, \tag{1}$$

$$\rho\left(\frac{\partial}{\partial t} + u\,\frac{\partial}{\partial x}\right)u + \frac{\partial p}{\partial x} = 0\,, \tag{2}$$

$$\frac{\rho}{\rho_0} = \left(\frac{c}{c_0}\right)^{2/(\gamma-1)} \quad \text{and} \quad \frac{p}{p_0} = \left(\frac{c}{c_0}\right)^{2\gamma/(\gamma-1)}\,, \tag{3}$$

where p denotes pressure, ρ denotes density, u denotes velocity, c denotes the speed of sound, γ denotes the ratio of the specfic heat capacities in constant pressure or volume processes (known as the adiabatic constant), and the subscript '0' denotes a reference value. The speed of sound, for an isentropic perfect gas, is given by

$$c^2 = \frac{\gamma p}{\rho}\,. \tag{4}$$

Combining equations (3) with equations (1) and (2) yields

$$\left(\frac{\partial}{\partial t} + u\,\frac{\partial}{\partial x}\right)c + \frac{\gamma-1}{2}\,c\,\frac{\partial u}{\partial x} = 0\,, \tag{5}$$

$$\left(\frac{\partial}{\partial t} + u\,\frac{\partial}{\partial x}\right)u + \frac{2}{\gamma-1}\,c\,\frac{\partial c}{\partial x} = 0\,. \tag{6}$$

Expressing $c = g(u)$, where $g(\cdot)$ is an unknown function, and substituting into equations (5) and (6), leads to the solution

$$c = c_0 \pm \left(\frac{\gamma-1}{2}\right)u\,, \tag{7}$$

where $c = c_0$ when $u = 0$.

On substituting equation (7) back into the continuity equation (5), or momentum equation (6), leads to the reduced wave equation (Hamilton and Blackstock [6], Chapter 1, equation 28, p.11):

$$\frac{\partial u}{\partial t} + (\beta u \pm c_0)\,\frac{\partial u}{\partial x} = 0\,, \tag{8}$$

where $\beta = (\gamma+1)/2$.

The Poisson solution for outward waves is

$$u = f\left[x - (c_0 + \beta u)\,t\right]\,, \tag{9}$$

where $f(\cdot)$ is any arbitrary function ([6], Chapter 1, equation 29, p.11).

On a wavefront, the propagation velocity is given by

$$\left.\frac{\mathrm{d}x}{\mathrm{d}t}\right|_{u=\text{constant}} = c_0 + \beta\, u = c + u\,, \tag{10}$$

from equation (7).

For a coordinate $\bar{x}$ moving at velocity c_0 in the positive x-direction, equation (8) can be expressed as

$$\frac{\partial u}{\partial t} + \beta\, u\, \frac{\partial u}{\partial \bar{x}} = 0\,. \tag{11}$$

Then equation (11) may be written in terms of the pressure perturbation

$$p' = \rho_0 c_0^2 \left[\frac{u}{c_0} + \frac{\beta}{2} \left(\frac{u}{c_0} \right)^2 + \ldots \right]\,, \tag{12}$$

where $p' = p - p_0$ ([6], Chapter 4, equation 17, p.71).

Although the waves have finite amplitude, on assuming that terms of $\mathrm{O}((u/c_0)^2)$ can be neglected, then $p' \approx \rho_0 c_0\, u$, and equation (11) is rewritten as

$$\frac{\partial p'}{\partial t} + \frac{\beta}{\rho_0 c_0}\, p'\, \frac{\partial p'}{\partial \bar{x}} = 0\,. \tag{13}$$

Equation (13) is the same as the lossless Burgers equation in one-dimensional form. McAlpine and Fisher [4] expressed this in non-dimensional variables as

$$\frac{\partial P}{\partial T} + \frac{2\pi}{B} P \frac{\partial P}{\partial X} = 0\,, \tag{14}$$

for non-dimensional time $T = c_0 t/\lambda$, distance $X = (2\pi/B)\,(\bar{x}/\lambda)$ and acoustic pressure $P = (\beta/\gamma)\,(p'/p_0)$, where $\lambda = \pi D/B$ is the shock spacing for a regular sawtooth waveform with B shocks (equal to the number of fan blades), and D is the diameter of the cylindrical intake duct.

B. Application to the nonlinear propagation of a sawtooth waveform in a cylindrical intake duct

1. Analytical methods

Figure 1 is an illustration of the characteristic helical path (in the x-direction) along which the pressure field advances inside a cylindrical intake duct. The non-dimensional time T, known as the

"Time of Flight", is related to the axial distance z by

$$T = \frac{c_0 t}{\lambda} = \frac{z}{D} K \,, \tag{15}$$

where K is

$$K = \frac{B}{\pi} \frac{M_{rel}^4}{\sqrt{M_{rel}^2 - 1}} \left(M_a \sqrt{M_{rel}^2 - 1} - M_t \right)^{-2} , \tag{16}$$

and $M_{rel} = \sqrt{M_a^2 + M_t^2}$ relates the relative Mach number to the axial Mach number M_a and the fan tip Mach number M_t. Equations (15) and (16) were derived first by Morfey and Fisher [3].

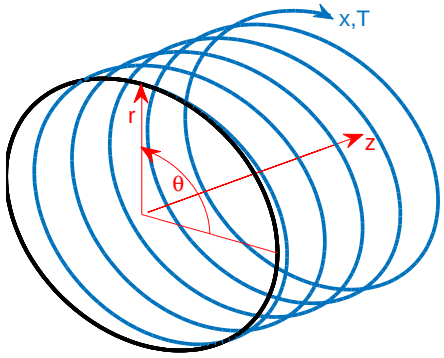

Fig. 1 Illustration of the helical path traced out by the sawtooth waveform inside a cylindrical intake duct.

In McAlpine and Fisher [11], equation (14) was solved for a regular sawtooth waveform by expressing

$$P(X,T) = \sum_{m=-\infty}^{\infty} C_m(T) \mathrm{e}^{\mathrm{i}mX} \,, \tag{17}$$

in terms of a complex Fourier series. The Fourier coefficients are given by

$$C_m = \frac{\mathrm{i}}{2\pi} \left(\frac{B}{m} \right) \left(\frac{\Delta p_s}{p_0} \right) \cos \frac{m\pi}{B} \,, \tag{18}$$

where Δp_s denotes the amplitude of each shock, and m is equal to an integer multiple of B (otherwise the coefficients equal zero). The differential equation obtained by substituting equations (17) and

(18) into equation (14), can be solved to yield an equation which describes the shock amplitude decay as

$$\Delta p_s(T) = \frac{p_0 s}{1 + (\beta/\gamma)\, T\, s}\,, \tag{19}$$

where $s = \Delta p_s(0)/p_0$ is the (non-dimensional) initial shock strength, i.e. at $T = 0$. Equation (19) also was first presented, albeit via an alternative derivation, by Morfey and Fisher [3]. It is applicable to predict the nonlinear decay for a regular sawtooth waveform propagating against a uniform oncoming flow inside a rigid cylindrical intake duct.

However, modern intake ducts contain acoustic liners fitted on the duct walls. Also in McAlpine and Fisher [11], the nonlinear propagation of a regular sawtooth waveform in an acoustically-lined duct was considered. A simple analytic expression to describe the shock amplitude decay, similar to equation (19), was derived for a regular sawtooth, utilizing a constant absorption rate, denoted by σ_B, for the BPF tone and all its harmonics. The shock amplitude decay is written as

$$\Delta p_s(T) = \frac{p_0 s\, \mathrm{e}^{-\sigma_B T}}{1 + (\beta/\gamma)\, T\, s \left[\left(1 - \mathrm{e}^{-\sigma_B T}\right)/\sigma_B T\right]}\,. \tag{20}$$

Equation (20) is applicable to predict the nonlinear decay for a regular sawtooth waveform propagating against a uniform oncoming flow inside a lined cylindrical intake duct, albeit all the harmonics of the pressure waveform are attenuated by the liner at the same rate, thus ensuring that a regular sawtooth is maintained throughout the propagation.

In reality, fan blades are not exactly alike due to small blade-to-blade differences. This will cause an irregular sawtooth waveform to be formed for any real fan blade set. Unlike a regular sawtooth waveform which contains harmonics at multiples of the blade passage frequency only, an irregular sawtooth waveform contains harmonics at multiples of the engine's shaft rotation frequency $\mathcal{F}$, known as the engine order tones (EO $= f/\mathcal{F}$). Owing to the small blade-to-blade differences, which cause the shocks to vary blade-to-blade, this means that the nonlinear propagation process is much more complex with interactions between all the engine order harmonics. Expressions similar to equations (19) and (20) cannot be easily derived for the nonlinear decay of an irregular sawtooth waveform. Additonally, a key issue is to include the frequency dependence of the acoustic liner attenuation.

2. Time-domain method

A time-domain method can be employed to simulate the nonlinear propagation of a sawtooth waveform. The application of the time-domain method is appropriate for modelling the rotor-locked pressure field and buzz-saw noise prediction in a rigid cylindrical intake duct. This type of approach has been used by other authors, including Fisher *et al.* [19], McAlpine and Fisher [4] and Uellenberg [20].

Calculation of the evolution of an irregular sawtooth inside a rigid intake duct must ensure that the gradual distortion of the pressure waveform is represented with sufficient accuracy. The nonlinear propagation and decay of each of the shock waves must be captured. This is achieved by using the following weak-shock equations [6, 11]

$$v_s = c_0 + \frac{\beta}{\rho_0 c_0} p_{s_m}' \,, \tag{21}$$

$$v_e = c_0 + \frac{\beta}{\rho_0 c_0} p_e' \,, \tag{22}$$

where v_s and v_e are the velocity of a shock or a point on an expansion wave. These are related directly to the mid-point pressure of the shock, p_{s_m}', or the pressure on the specific point of the expansion wave, p_e'. Also it is reiterated that the pressure p' denotes the deviation in the pressure from the mean static pressure p_0.

Equations (21) and (22) correspond directly to equation (10) from the theory of one-dimensional nonlinear waves. These equations can be used to track the nonlinear distortion of the whole waveform by evaluating how each point on the waveform varies with time. Then this is linked to propagation within a cylindrical intake duct, via the "Time of Flight" T (equation (15)) which directly links the helical path to the axial distance.

Modelling the irregular sawtooth, it is assumed that the inter-shock expansion waves are always linear. Figure 2 gives an illustration of the nonlinear propagation and shock attenuation process. Owing to the fact that the expansion waves are taken to be linear, the propagation is rapid to compute for each time step, since only two points at the ends of each expansion wave and a midpoint for each shock wave, are required to fully define the waveform. For example, consider a shock wave centered about the mean static pressure p_0, see figure 2(a). The shock wave travels at $v_s(p_{s_m}')$

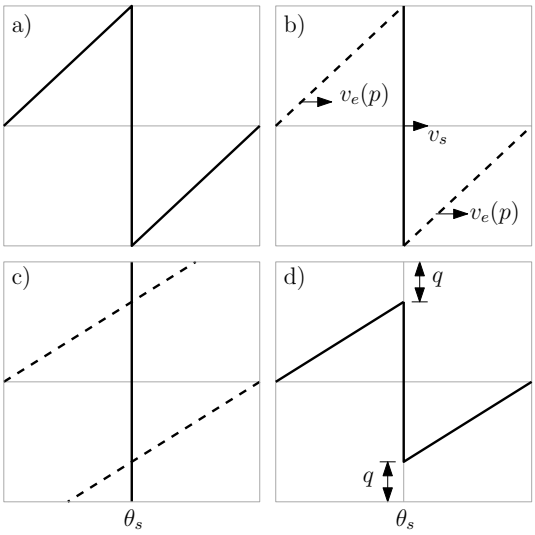

Fig. 2 Illustration of the propagation and decay of a single N-wave, with mid-point pressure equal to the reference (mean) pressure. In this moving reference frame, the position of the shock, θ_s, does not vary, but the shock amplitude is attenuated at its high- and low-pressure sides (shown by q).

(equation(21)), whereas points on the expansion wave travel at $v_e(p'_e)$ (equation(22)), see figure 2(b). In this simple example $p_{s'_m} = 0$. Points where the pressure $p'_e > p_{s'_m}$ travel faster than the shock, whereas points where the pressure $p'_e < p_{s'_m}$ travel slower than the shock. After an arbitrary time step, Δt, the waveform looks as illustrated in figure 2(c). The intersection points between the expansion waves and the shock wave is resolved, and the attenuated shock is then corrected as shown in figure 2(d). The change in the amplitude is q at both the high and low pressure sides of the shock. For an irregular sawtooth, the same process applies. The attenuation will be different at the high and low pressure sides of the shocks. In addition to the nonlinear attenuation, the shocks will propagate at different velocities relative to each other, so the time-domain algorithm is programmed to correct for merging shock waves, and crossover of the first and last shock of the waveform, owing to 2π-periodicity.

3. Frequency-domain method

Alternatively a frequency-domain method can be employed to simulate the nonlinear propagation of a sawtooth waveform. Modern intake ducts have acoustic linings installed on the duct wall. The acoustic liners can be tuned to target a prescribed frequency range [21]. In fact it is not uncommon to have a liner installed close to the fan followed by a different liner which covers the rest of the lined area inside the intake barrel. High-amplitude low-frequency tones could be targeted close to the fan, whereas further upstream of the fan, the aim is to attenuate the higher-frequency sound [21]. Therefore, propagation models for realistic intake ducts must take into account the nonlinear attenuation of the shock waves and the effect of sound absorption by the installed acoustic liners.

The benefit of transforming the problem to the frequency domain, vis-à-vis using the time-domain method, is that absorption by acoustic liners can be more easily incorporated into the computational model. Thus, application of the frequency-domain method is appropriate for modelling the rotor-locked pressure field and buzz-saw noise prediction in a lined cylindrical intake duct.

The frequency-domain method has been developed extensively by McAlpine *et al.* [4, 11–14]. In brief, the evolution of an irregular sawtooth inside a lined intake duct is modelled by Burgers equation, which describes nonlinearity and dissipation. Equation (14) is the lossless form of Burgers equation, expressed in dimensionless parameters. Inclusion of the diffusive term gives

$$\frac{\partial P}{\partial T} + \frac{2\pi}{B} P \frac{\partial P}{\partial X} = \frac{\varepsilon}{B^2} \frac{\partial^2 P}{\partial X^2} \,, \tag{23}$$

where ε is the *dissipation constant* (defined in references [11–13] based on the nonlinear attenuation of a regular N-wave), explicitly included to dissipate energy, particularly at high frequencies. The effect of absorption by the acoustic liner is modelled by modifying the coupled spectral differential equations, obtained on substituting $P\,(X,T)$ from equation (17) into equation (23), by noting that in linear acoustics the Fourier harmonics C_m should satisfy

$$\mid C_m(T) \mid \;\; = \;\; \mid C_m(0) \mid \exp\{-\sigma(m)T\} \,, \tag{24}$$

where $\sigma\,(m)$ is the liner absorption or linear decay rate associated with harmonic order m. Accord-

ingly, with the inclusion of the numerical dissipation term and the linear attenuation term, in the frequency domain it is required to solve:

$$\frac{\mathrm{d}C_m}{\mathrm{d}T} = -\frac{\mathrm{i}m\pi}{B}\left(\sum_{l=1}^{m-1} C_{m-l}C_l + 2\sum_{l=m+1}^{N} C_l\widetilde{C}_{l-m}\right) - \varepsilon\,\frac{m^2}{B^2}\,C_m - \sigma(m)\,C_m\,. \tag{25}$$

It is well known that time-harmonic "spinning" pressure modes $\hat{p}\exp\{\mathrm{i}\omega t\}$ in a cylindrical duct can be expressed, in the cylindrical polar coordinate system (r,θ,z), in the form

$$\hat{p}_{mn}(r,\theta,z) = A_{mn}\mathrm{J}_m(\kappa_{mn}r)\exp\left[\mathrm{i}\left(-k_{z\,mn}z \pm m\theta\right)\right]\,, \tag{26}$$

where $\hat{p}_{mn}$ denotes mode "(m,n)". The modal amplitude A_{mn} is a constant, and J_m is the Bessel function of the first kind of order m. The modal solution (26) has azimuthal and axial wavenumber m and $k_{z\,mn}$ respectively, and radial eigenvalues denoted by κ_{mn}. These are linked via the dispersion relation

$$k_{z\,mn} = \frac{k}{1-{M_a}^2}\left\{-M_a \pm \left[1-\left(1-{M_a}^2\right)\left(\frac{\kappa_{mn}}{k}\right)^2\right]^{1/2}\right\}\,. \tag{27}$$

Since the rotor-locked pressure field is steady in the frame of reference rotating with the fan, the azimuthal phase velocity of the steady modes $\omega/m = 2\pi\mathcal{F}$, which means that m corresponds to the EO, i.e. the dimensionless frequency representing each harmonic of the shaft rotation, known as the engine order.

The linear decay rate $\sigma(m)$ is dependent upon mode number (or frequency), and is given by

$$\sigma(m) = -\frac{k_{zi}D}{K}\,, \tag{28}$$

where k_{zi} is the imaginary part of the axial wavenumber for the mode $(m,1)$. Thus the liner absorption is based on taking the least attenuated mode at each azimuthal order. Scattering at rigid/lined duct wall discontinuities is not included in the modelling.

In a lined duct, the modes can be calculated using a wall boundary condition based on the lining's specific acoustic impedance. Standard acoustic liner impedance models exist which take into account the flow conditions over the lining and the structure of the acoustic liner. Acoustic liners are mostly arranged in single-layer or double-layer configurations, where each layer is comprised of a facing-sheet which covers a honeycomb structure comprised of multiple small cavities. Liner

performance can be quantified by calculating the linear decay rates for a specified frequency range. Factors which can affect the liner absorption include the effective open area of the facing sheet, the liner's depth, and the grazing flow over the lining including the duct wall boundary layer.

In the benchmarking results in section IV C, a simple model of the (non-dimensional) specific acoustic impedance Z for a single-layer cavity lining is employed, viz.

$$\frac{Z}{\rho_0 c_0} = R + \mathrm{i}\,[X_m + X_c]\ , \tag{29}$$

where the non-dimensional resistance R is constant, and the non-dimensional reactance X is the sum of the face-sheet mass reactance X_m and the cavity reactance $X_c = -\cot(kh)$, where h is the cavity depth. Equation (29) is given in the review of duct acoustic treatments by Motsinger and Kraft ([22], p.176, Eq. (5)).

However, for the validation results in section IV D, a proprietary double-layer cavity lining was installed in the rig-scale fan test. The specific acoustic impedance could be described by the model given in Motsinger and Kraft for a double-layer cavity lining ([22], p.177, Eq. (6)), or an extension of the semi-empirical liner impedance model for a single-layer liner by Murray and Astley [23]. However, for the purpose of the validation of the propagation method, predictions of the liner impedance were obtained from a Rolls–Royce proprietary method, that has been validated separately based on in-situ impedance measurements for this type of liner construction. It is noted that some liner impedance models can include nonlinear effects owing to high-amplitude sound fields, but integrating a nonlinear lining model into the nonlinear propagation simulations has not yet been investigated by the authors.

An in-house code (not discussed) that calculates the modes in a cylindrical duct containing uniform mean flow, utilising the Ingard–Myers acoustic boundary condition [24], is used to evaluate the modal decay rates used in this study. The inclusion of the term $-\sigma\,(m)\,C_m$ in equation (25) enables the absorption of sound by the acoustic liner to be modelled. It is also noted that this term can be utilised to enable duct mode cut-off to be modelled, using this frequency-domain method.

III. Time-frequency domain method

The propagation of buzz-saw noise is the combination of the non-linear propagation and attenuation of the shocks in conjunction with absorption by the acoustic lining. The time-domain method presented in section II B 2 is able to provide an accurate description of the non-linear propagation (albeit for linear profiles of expansion waves only) but it is not possible to easily include the liner absorption. Time domain impedance modelling is still relatively limited. On the other hand, the frequency-domain method outlined in section II B 3 can more readily include the frequency-dependent liner absorption but the non-linear propagation is more cumbersome to describe in this framework as there is no general expression for the exact amount of damping required. It is then natural to develop a combination of these two schemes whereby the non-linear propagation and attenuation are described in the time domain whilst the liner absorption is modelled in the frequency domain. This is referred to as the hybrid approach [6] or a modified weak-shock theory [18]. This strategy is now described and verified.

A. Numerical time-domain model

The semi-analytical time-domain model outlined in section II B 2 was limited to linear expansion waves. To remove this constraint a more general numerical method, based on a semi-Lagrangian scheme, is used. The solution $P(X,T)$ of the problem is discretised both in space and time. The spatial coordinate X is described using a uniform grid between 0 and 2π. The grid point coordinates are given by $X_j = j\Delta X$ where $j = 0, ..., N-1$ and $\Delta X = 2\pi/N$ is the grid spacing. Starting from an initial solution at $T = 0$, the solution is marched in time with a time step ΔT. The value of pressure for the jth grid point at the nth time step is denoted $P_j^n = P(X_j, n\Delta T)$.

The left-hand side of equation (23) is essentially a transport equation where the advection velocity is a function of the solution P. Lagrangian numerical schemes are specifically designed for this class of problems. To calculate the solution at the next time step, the first stage in a Lagrangian method is to move the grid points according to the advection velocity. From equation (23) we can see that the convection velocity of a point on the waveform is $2\pi P/B$. When written in non-dimensional

form this shows that the solution at each grid point X_j is expected to move to

$$Y_j = X_j + \frac{2\pi}{B} P_j^n \Delta T \ , \tag{30}$$

over a time interval ΔT. The combination of the new grid points Y_j and pressure values P_j^n provides a description of the new solution at time step $n+1$, as illustrated in figure 3.

The issue is that the new grid points Y_j are different from the uniform grid X_j initially defined. This could be problematic as it becomes difficult to maintain a sufficient grid resolution everywhere in the domain. In addition the introduction of sound absorption by the acoustic lining (described in the next section) requires a Fourier transform which is more expensive to calculate on a non-uniform grid. This can be avoided by defining the solution P_j^{n+1} at the new time step as the interpolation of the solution P_j^n at the grid points Y_j back onto the original grid X_j. A linear interpolation is used for this purpose.

A key point of this interpolation is the treatment of the shocks. The solution defined by the values P_j^n at the point Y_j can become multi-valued near a shock, as illustrated in figure 3 (unless the time step ΔT is very small). This is because the high-pressure point of the shock will necessarily move faster than the low-pressure point. This can be easily detected by finding the grid point k for which $Y_k > Y_{k+1}$ and the position of the shock is then defined as $\overline{Y} = (Y_k + Y_{k+1})/2$. To construct the solution at time $n+1$, the expansion wave to the left of the shock (for $j \leq k$) is used to interpolate the solution at the points $X_j < \overline{Y}$. The expansion wave to the right of the shock (for $j > k$) is used to interpolate the solution at the points $X_j > \overline{Y}$. This process, illustrated in figure 3, will naturally reduce the amplitude of the shock and represents the non-linear decay of the waveform.

To avoid multi-valued solutions, it is possible to impose a restriction on the time step ΔT similar to the Courant–Friedrichs–Lewy (CFL) condition. Based on the advection velocity given in equation (23) the time step should be selected such that [6]

$$\frac{\Delta X}{\Delta T} > \max(P_j^n - P_{j-1}^n)\frac{2\pi}{B} \ . \tag{31}$$

The maximum time step is therefore controlled by the largest shock amplitude in the waveform.

Note that the coordinate X is considered periodic and there is therefore no boundary condition

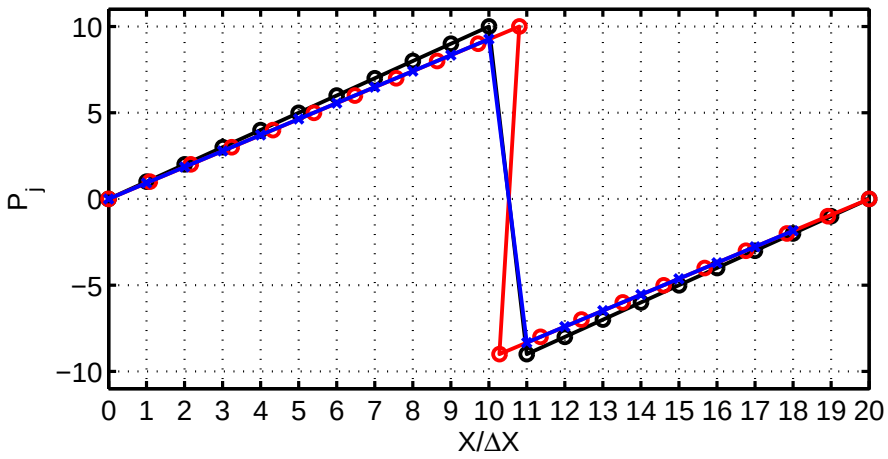

Fig. 3 Example of calculation between two time steps. Black: solution at time step n with pressure values P_j^n at the grid points X_j. Red: solution at the time step $n+1$ based on the pressure values P_j^n at the points Y_j (note the multi-valued region at the shock). Blue: actual solution at time $n+1$ with pressure values P_j^{n+1} at grid points X_j.

to apply at $X = 0$ and $X = 2\pi$. However, when calculating the new grid points Y_j it is necessary to ensure that any point leaving the range $0 \leq X < 2\pi$ are moved back to the correct position within this range to enforce the periodic nature of the solution.

A key difference with the time-domain model described in section II B 2, is that the shocks are not described as discontinuities but instead they have a finite width dictated by the grid resolution ΔX. It is therefore important to use a fine spatial resolution. In particular if the grid resolution is not sufficient the attenuation of the shocks will be overestimated. An overview of the effect of grid resolution and convergence of results is discussed in section III C.

B. Frequency-domain liner absorption implementation

In conjunction with the non-linear propagation modelled by the semi-Lagrangian scheme outlined above, an additional step is included to model the liner absorption. As discussed in section II B 3, the attenuation of the sound field is best described in terms of duct modes of azimuthal order m. The solution $P(X,T)$ can be related to these azimuthal modes after a Fourier transform, as defined by equation (17).

After the solution at time step n is obtained, and before calculating the next time step, the

Fourier harmonics C_m are calculated from the values P_j^n of pressure using (17). They are then scaled based on the attenuation rate of the corresponding acoustic duct modes [18, 25, 26] to give:

$$C_m \exp\{k_{zi}\Delta z\} = C_m \exp\left\{-\sigma(m)\frac{K}{D}\Delta z\right\} = C_m \exp\{-\sigma(m)\,\Delta T\}\ , \tag{32}$$

following equations (15) and (28). The axial distance covered by the wavefront over an interval ΔT is given by $\Delta z = \Delta T(D/K)$.

Once the Fourier harmonics C_m have been scaled, they are converted back to a pressure distribution P_j^n using an inverse Fourier transform.

To improve the speed of the algorithm the number N of grid points is taken to be a power 2 so that the Fast Fourier Transform can be used without padding. Furthermore, performing two Fourier transforms at each time step would be too costly. The application of the liner attenuation does not have to be applied at every time step. As suggested by Pestorius [18], it can be applied every M time steps and the cumulative effect of the liner is applied by using the axial distance $\Delta z = M\Delta T(D/K)$ covered in the time interval $M\Delta T$. Guidelines to select a suitable value for M will be discussed in the next section.

C. Code verification

We now illustrate how an implementation of the hybrid model can be verified. To demonstrate grid convergence we consider the propagation of a regular waveform with 20 shocks, linear expansion waves and no liner attenuation. A fixed time step has been used throughout. The exact solution for this case has been outlined in section II B 1. The numerical error is calculated on the complex-valued amplitudes of the Fourier harmonics C_m. The error is defined as

$$\text{error} = \sqrt{\frac{\sum_m |\mathcal{C}_m - C_m|^2}{\sum_m |C_m|^2}}\ , \tag{33}$$

where $\mathcal{C}_m$ are the Fourier harmonics obtained at each grid resolution, and C_m are the corresponding harmonics obtained from the analytic solution.

Figure 4 shows the numerical error calculated at different axial stations along the duct and as a function of the grid resolution expressed as $\bar{N} = \log_2\left(N\right)$ such that $N = 2^{\bar{N}}$. The grid convergence of the model is well demonstrated and the increase in numerical error for longer propagation distances

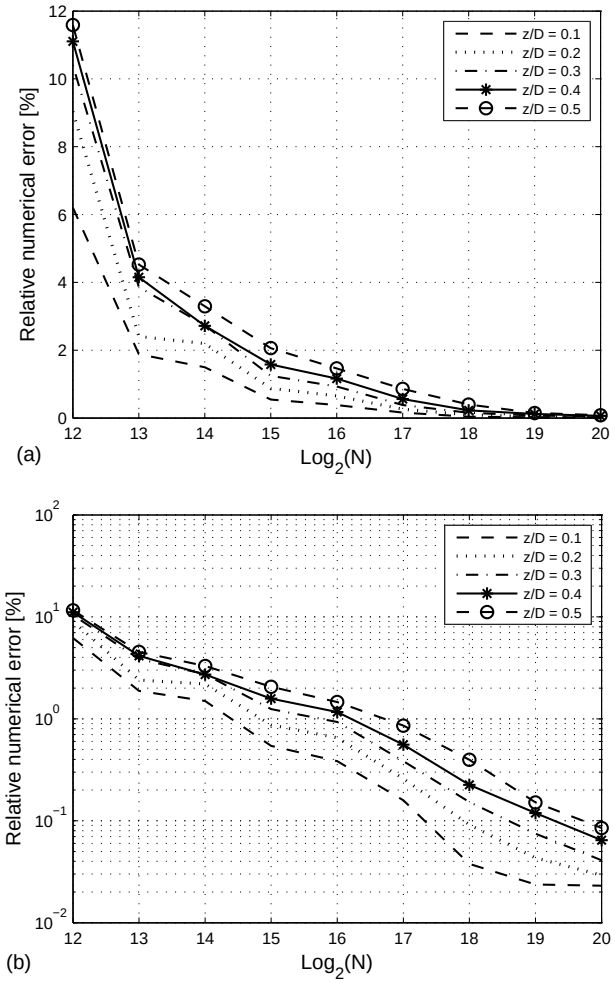

Fig. 4 Relative numerical error shown on a linear scale (a) or logarithmic scale (b) for the propagation of a regular sawtooth in a rigid duct for various grid resolutions. Example for a sawtooth with 20 shocks and initial shock strength $s = 0.432$.

is also clearly visible. As $\bar{N}$ increases, the percentage error reduces over the entire distance which is propagated owing to the finer grid.

These results indicate that a grid with $\log_2(N) \geq 17$ will maintain the error below 1% over a propagation distance of a duct radius $D/2$. While an error of 1% in linear scale might be considered too stringent for acoustic levels, one should keep in mind that the non-linear propagation of buzz-saw noise is particularly sensitive to small changes in the solutions and it is therefore important to minimise the numerical error.

For a lined duct one can choose the parameter M controlling the interval between two appli-

cations of the liner damping. The impact of this parameter is assessed with the same test case as above but the liner is described using the same attenuation rate, 9 dB/radius, for all the azimuthal orders (i.e. $\sigma(m)$ in equation (32) is independent of m). In this example the parameter M is chosen so that the liner attenuation is applied regularly after the waveform has propagated a distance $\Delta z = 0.0006D$, $0.006D$ and $0.06D$. Figure 5 show the evolution of the amplitude of the BPF tone as the waveform propagates along the duct for these three values of Δz. The inclusion of the liner attenuation is clearly visible, especially for the two largest values of Δz considered. For the largest value, the prediction deviates significantly from the theoretical solution. For $\Delta z = 0.006D$ the overall rate of decay of the tone is well represented, but the interval between two applications of the liner attenuation is still large enough to create significant discrepancies compared with the exact solution. Finally the smallest value of Δz provides the result where there are no discernable differences compared with the exact solution.

The results presented in this section serve as examples of verification and one should perform a similar study for the specific problem at hand in order to identify the parameters that provide the required level of accuracy whilst minimising the computational cost.

IV. Benchmark and validation results

Computational results obtained with the time-frequency domain method are benchmarked against the analytic solution for a regular sawtooth waveform (section II B 1), and numerical simulations for an irregular sawtooth waveform using the time-domain method (section II B 2) or frequency-domain method (section II B 3). For convenience, the one-dimensional nonlinear propagation time-frequency domain method will be hereafter referred to by the acronym 1DNP–TFD. The time- and frequency-domain numerical solutions will be referred to by the acronyms TDNS and FDNS which were used by McAlpine & Fisher [4]. Results are compared with benchmark solutions, at several axial stations, in an intake containing a fan with 20 blades ($B = 20$). For all the results, typical irregular sawtooth waveforms, similar to the real-life rotor-locked pressure field close to the fan, were used in the simulations. For easy reference, the irregular sawtooth waveforms will be referred to as IR_1 and IR_2. The waveform IR_2 has, initially, higher levels of shock-to-shock differences compared to IR_1, in order to test the performance of the model for two different scenarios. The two irregular

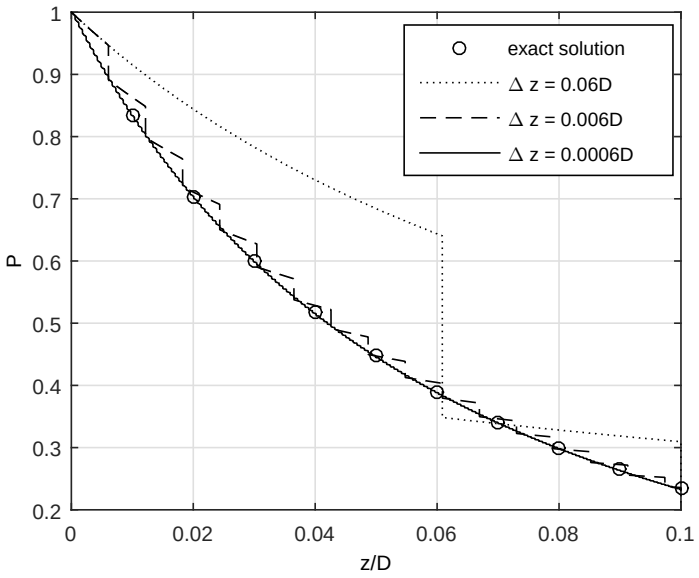

Fig. 5 Amplitude of the BPF tone as a function of axial position for a regular sawtooth waveform in a lined duct. Example for a sawtooth with 20 shocks, initial shock strength $s = 0.432$ and constant liner absorption rate.

sawtooth waveforms, IR_1 and IR_2, were constructed from a base regular sawtooth with 9% and 12% variation of shock amplitude and 0.3% and 2% shock spacing variation respectively. Also an illustrative validation example is included, showing comparison of rig-scale test measurements with predictions using the 1DNP–TFD code.

A. Comparison with analytic solution

Figures 4 and 5 have already shown how the 1DNP–TFD code compares with the analytic benchmark solutions. To further emphasize the good agreement between the results, figure 6 shows the comparison for the first 10 BPF harmonics for a regular sawtooth pressure waveform propagating in a rigid or lined cylindrical intake duct. The dashed lines show the analytic solutions (equations (19) or (20)), and the symbols show the results from the 1DNP–TFD code at axial stations $z/D = 0$, 0.1, 0.2 and 0.3. At each BPF harmonic, the time-frequency domain method accurately predicts the nonlinear decay of each tone, based on the propagation of a regular sawtooth pressure waveform.

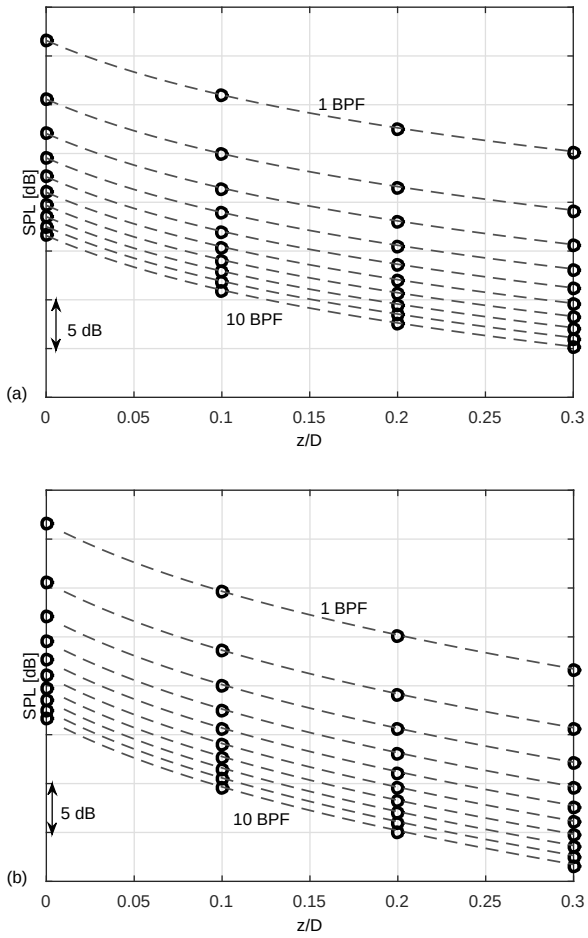

Fig. 6 Comparison of the amplitudes of the first ten BPF harmonics for a regular sawtooth in a rigid duct (a) and a lined duct with a constant liner absorption rate (b). Key: Symbols—Numerical results; Dashed lines—Analytic solutions.

B. Comparison with time-domain method and frequency-domain method: rigid duct

The time-domain method is only applicable for nonlinear propagation simulations in a rigid cylindrical intake duct. Results obtained with the time-frequency domain method (1DNP-TFD) compared against benchmark solutions from the time-domain method (TDNS) and frequency-domain method (FDNS) are shown in figures 7–10. Very good agreement between the results calculated by the three different methods is observed, both on comparing the pressure waveforms and the EO frequency spectra, over the propagation distance from $z/D = 0$ to 0.5 which is a typical intake duct length. There are no significant differences between the sets of results up to axial

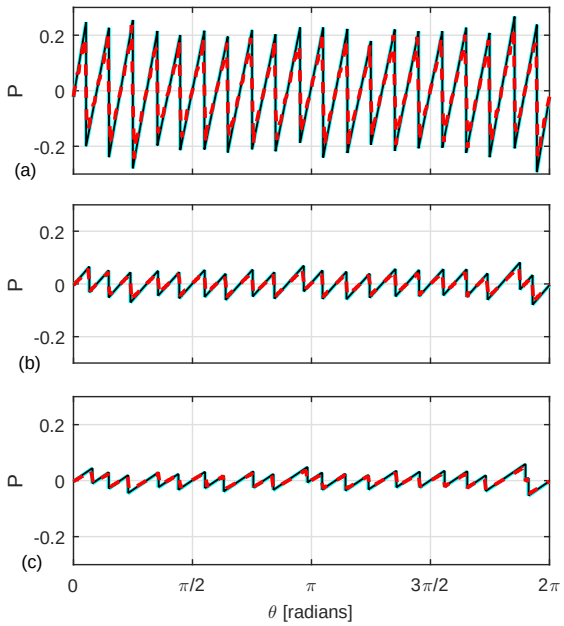

Fig. 7 Comparison between numerical results from the TDNS, FDNS and 1DNP–TFD codes. Simulation of irregular sawtooth pressure waveform $\underline{\mathrm{IR}_1}$ in a rigid cylindrical intake duct: (a) $z/D = 0$, (b) $z/D = 0.25$, and (c) $z/D = 0.5$. Key: Blue line—TDNS; Red dashed line—FDNS; Black line—1DNP–TFD.

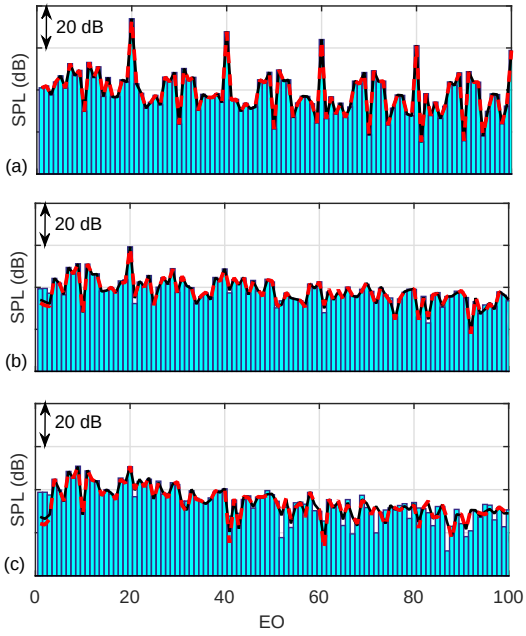

Fig. 8 Comparison between numerical results from the TDNS, FDNS and 1DNP–TFD codes. EO frequency spectrum for irregular sawtooth $\underline{\mathrm{IR}_1}$ in a rigid cylindrical intake duct: (a) $z/D = 0$, (b) $z/D = 0.25$, and (c) $z/D = 0.5$. Key: Blue bars—TDNS; Red dashed line—FDNS; Black line—1DNP–TFD.

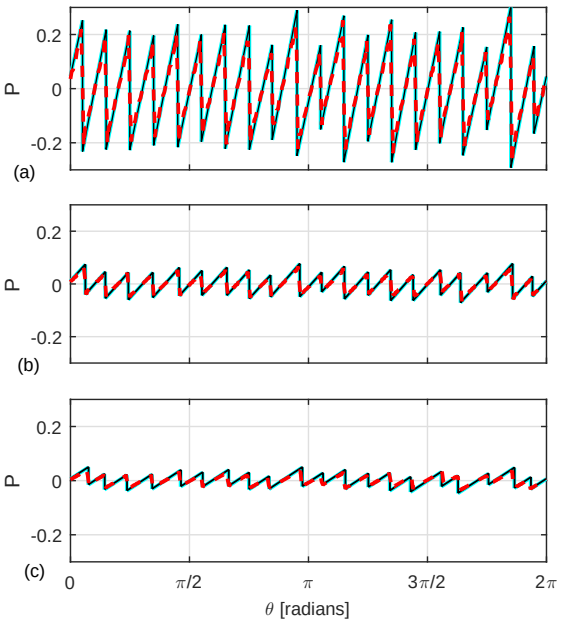

Fig. 9 Comparison between numerical results from the TDNS, FDNS and 1DNP–TFD codes. Simulation of irregular sawtooth pressure waveform $\underline{\mathrm{IR}_2}$ in a rigid cylindrical intake duct: (a) $z/D = 0$, (b) $z/D = 0.25$, and (c) $z/D = 0.5$. Key: Blue line—TDNS; Red dashed line—FDNS; Black line—1DNP–TFD.

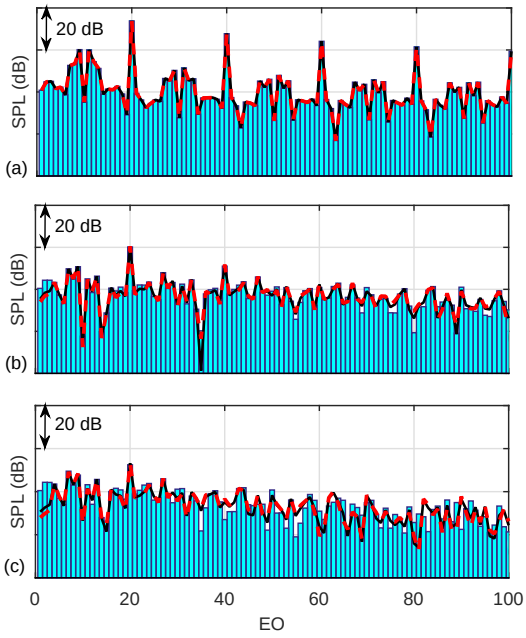

Fig. 10 Comparison between numerical results from the TDNS, FDNS and 1DNP–TFD codes. EO frequency spectrum for irregular sawtooth $\underline{\mathrm{IR}_2}$ in a rigid cylindrical intake duct: (a) $z/D = 0$, (b) $z/D = 0.25$, and $z/D = 0.5$. Key: Blue bars—TDNS; Red dashed line—FDNS; Black line—1DNP–TFD.

station $z/D = 0.25$ for both waveforms considered except for the cut-off tones EO1 to EO3 (spectra in figures 8(b) and (c), and 10(b) and (c)) which is not modelled in the time-domain propagation. Beyond this propagation range, slight tone-to-tone differences are observed as the effect on the low frequency cut-off modes become more visible in the frequency spectrum. It is important to note that the results of the models are the same if the cut-off modes are not considered. FDNS and 1DNP-TFD agree more closely for this reason. The waveforms generated by FDNS appear lower in amplitude when compared to the other two models due to the limited range of frequency employed in the reproduction of the waveform (spectra in figures 7(b) and (c), and 9(b) and (c)). Overall, the nonlinear attenuation of the waveforms is accurately predicted. It is emphasised that good agreement is observed for irregular sawtooth IR_1, which has small blade-to-blade differences, and also for irregular sawtooth IR_2, which has larger blade-to-blade differences, which causes more nonlinear distortion. From the comparison of benchmark results provided by the time-domain method, the time-frequency domain method is seen to accurately represent the nonlinear propagation of an irregular sawtooth pressure waveform, in the absence of absorption by acoustic lining, in a rigid cylindrical intake duct.

C. Comparison with frequency-domain method: lined duct

The frequency-domain method is applicable for nonlinear propagation simulations in rigid or acoustically-lined cylindrical intake ducts, albeit it was developed primarily to provide an engineering model capable of predicting the nonlinear attenuation and liner absorption in a lined intake. Hence, results obtained with the time-frequency domain method (1DNP-TFD) compared against benchmark solutions from the frequency-domain method (FDNS) provide simulations which incorporate nonlinear effects and the effects of acoustic liner absorption.

In order to generate simulations for an acoustically-lined intake duct, it is necessary to calculate the EO modes, and specifically their predicted linear decay rates, determined by calculating the axial wavenumbers of modes $(m, 1)$, where the azimuthal order m is equal to the engine order EO. Figure 11 shows a prediction of the linear decay rates used in the benchmark simulations. The liner impedance model was based on a single-cavity lining, with a porous face-sheet covering the honeycomb cavity layer (see equation (29) where values 3.75, 0.0125m and 4% are chosen for the

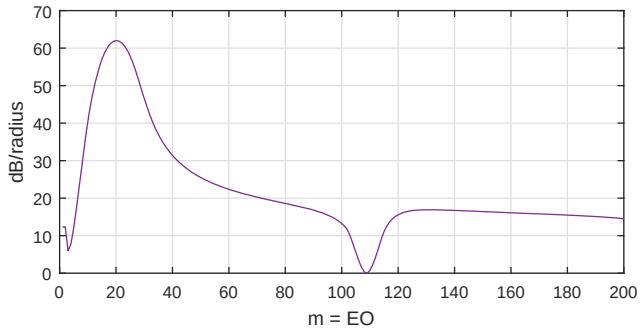

Fig. 11 Linear decay rates for engine orders 1 to 100.

resistance, cavity depth and porosity of the face-sheet respectively for an axial flow of Mach number 0.5).

As is seen in figure 11, this type of lining typically has a well-defined optimum frequency range, over which there is predicted high absorption. Outside this range, the absorption is predicted to be much less. This means that this type of lining can be tuned to a specific frequency range. In the examples shown for this benchmark case, the lining is optimised at around the blade passing frequency.

Results of the benchmarking are shown in figures 12–15. Note that the waveforms and spectra at the start, $z/D = 0$, are the same as the examples for IR_1 and IR_2, already shown in figures 7–10 for the simulations in the rigid cylindrical intake duct. Accordingly the results at the start are not shown in figures 12–15.

The comparison between the results calculated by the 1DNP-TFD and the FDNS codes show good agreement over the propagation distance from $z/D = 0$ to 0.5. The waveforms match quite well at each station. Comparing the sawtooth waveforms, there are observable differences in the resolution of the shocks calculated by the two methods. These differences are small, and it is emphasised that the nonlinear attenuation of the shocks is calculated differently by each of the models. However, comparing the spectra, from tone-to-tone only small differences are observed in the spectral comparisons. Overall there is good agreement between the time-frequency domain and frequency-domain methods at all the stations along the axis of the duct, with only minimal differences at some of the tones in the EO frequency spectrum.

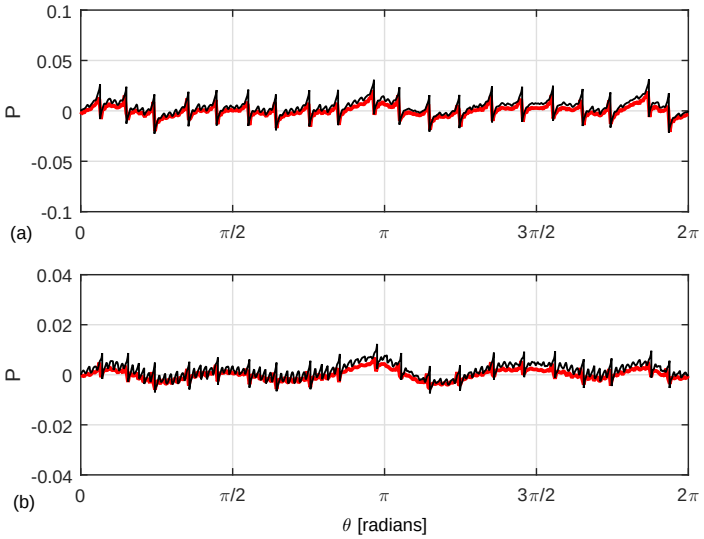

Fig. 12 Comparison between numerical results from the FDNS and 1DNP–TFD codes. Simulation of irregular sawtooth pressure waveform $\underline{\mathrm{IR}_1}$ in a lined cylindrical intake duct: (a) $z/D = 0.25$, and (b) $z/D = 0.5$. Key: Red line—FDNS; Black line—1DNP–TFD.

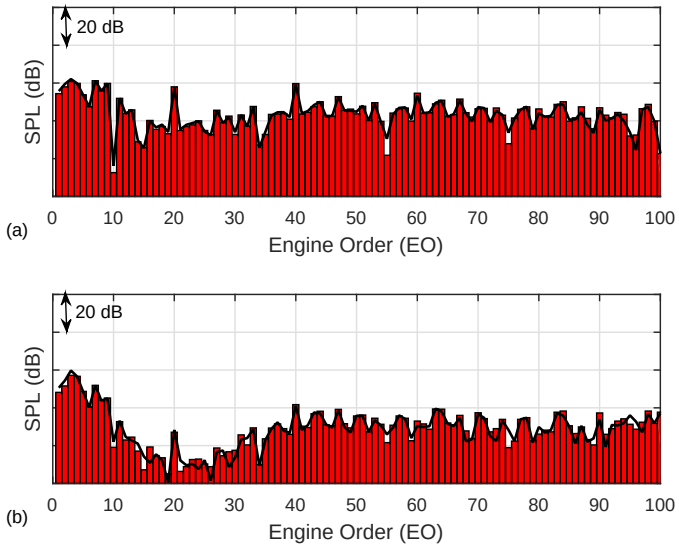

Fig. 13 Comparison between numerical results from the FDNS and 1DNP–TFD codes. EO frequency spectrum for irregular sawtooth $\underline{\mathrm{IR}_1}$ in a lined cylindrical intake duct: (a) $z/D = 0.25$, and (b) $z/D = 0.5$. Key: Red bars—FDNS; Black line—1DNP–TFD.

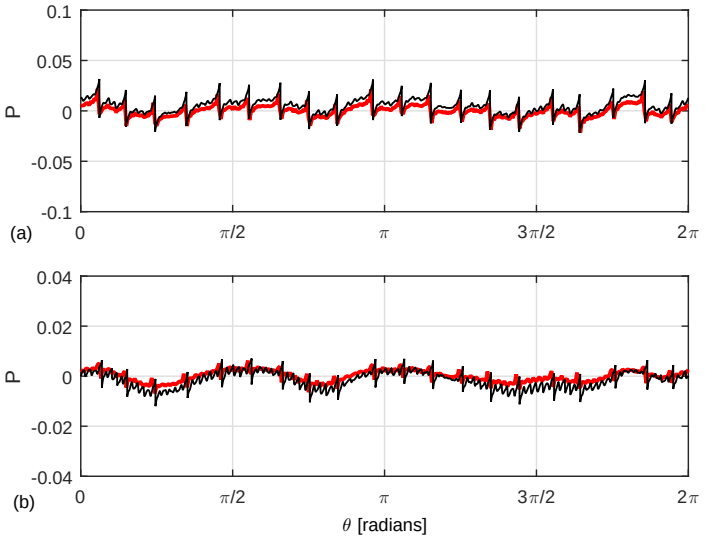

Fig. 14 Comparison between numerical results from the FDNS and 1DNP–TFD codes. Simulation of irregular sawtooth pressure waveform $\underline{\mathrm{IR}_2}$ in a lined cylindrical intake duct: (a) $z/D = 0.25$, and (b) $z/D = 0.5$. Key: Red line—FDNS; Black line—1DNP–TFD.

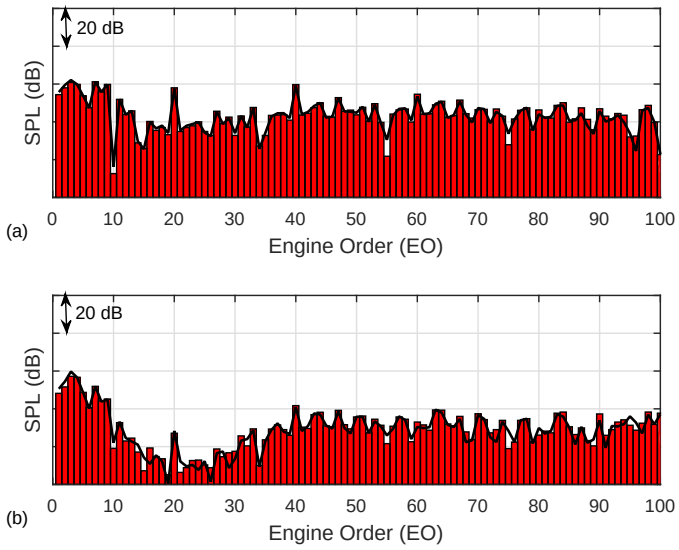

Fig. 15 Comparison between numerical results from the FDNS and 1DNP–TFD codes. EO frequency spectrum for irregular sawtooth $\underline{\mathrm{IR}_2}$ in a lined cylindrical intake duct: (a) $z/D = 0.25$, and (b) $z/D = 0.5$. Key: Red bars—FDNS; Black line—1DNP–TFD.

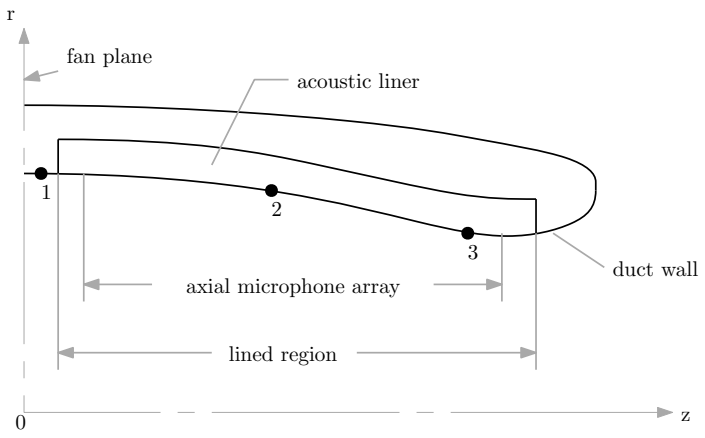

Fig. 16 Illustration of the rig-scale intake duct (not to scale).

The very fine grid used in the time-frequency domain code means that the shocks' peaks and troughs are better resolved compared to the results from the frequency-domain code. This is the case for both the sawtooth waveforms (IR_1 and IR_2). Similar levels of agreement in the two sets of results is observed for the two waveforms at each station, albeit the resolution of the nonlinear decay of the shocks is slightly better for the rigid intake. However, in the lined intake, the overall levels are lower owing to attenuation provided by the liner absorption. Hence, in the lined intake, the shocks' decay is much more compared to the shocks in the rigid intake, and also in the lined intake, the expansion waves have a characteristic wavy appearance. However, the levels of the tones are reliably predicted in the lined intake. It is noteworthy to point out that as seen in figure 11, there is about 60dB attenuation expected at the BPF over a axial distance equal to the radius which in addition to the nonlinear decay of the shock result in over 60dB attenuation of the tones around BPF. From figures 13(c) and 15(c), this amounts to the shock pressure amplitudes reduced to less than 0.1% of their initial value for both wave forms propagated. Hence, the good agreement between the models at $z/D = 0.5$ is remarkable.

D. Comparison with rig-scale measured data

For validation purposes, results from the time-frequency domain method are compared against measurements from a rig-scale fan test carried out by Rolls–Royce plc. Measurements were acquired for both rigid and lined intake wall configurations. A sketch of the model-scale rig intake showing

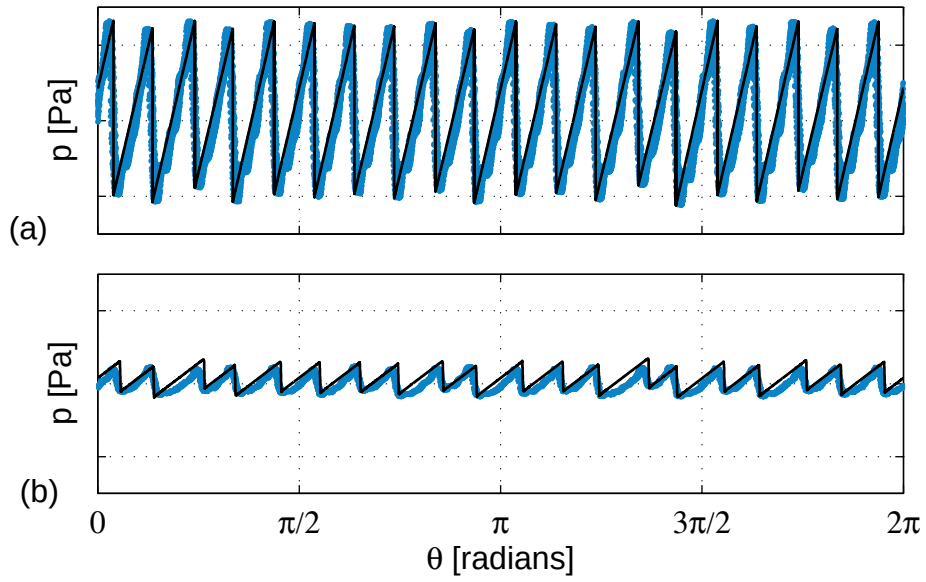

Fig. 17 Comparison between numerical results from the 1DNP-TFD code and measured data at (a) station 1 and (b) station 3. Sawtooth pressure waveform in the rigid intake duct. Key: Black line—1DNP–TFD; Blue line—data.

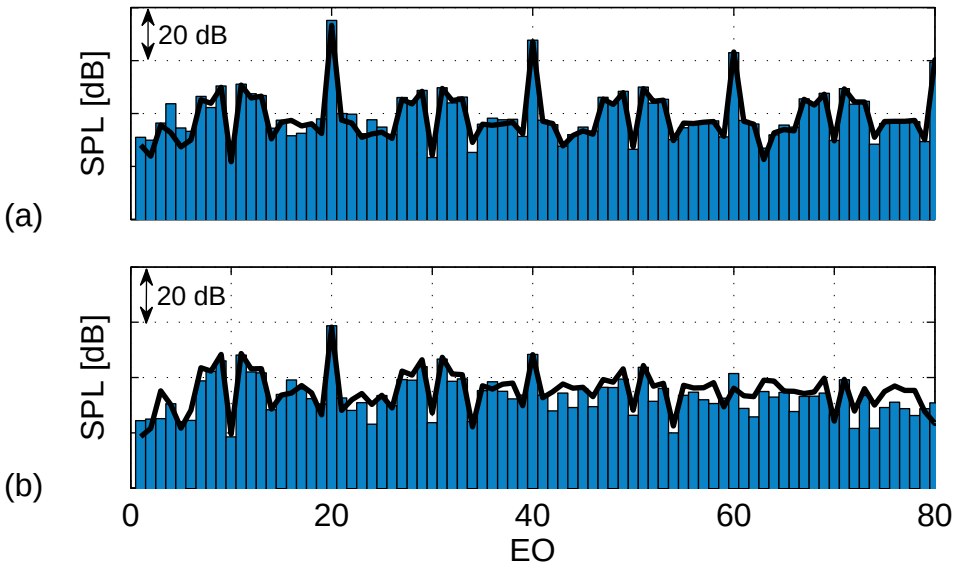

Fig. 18 Comparison between numerical results from the 1DNP-TFD code and measured data at (a) station 1 and (b) station 3. EO frequency spectrum in the rigid intake duct. Key: Black line—1DNP–TFD; Blue bars—data.

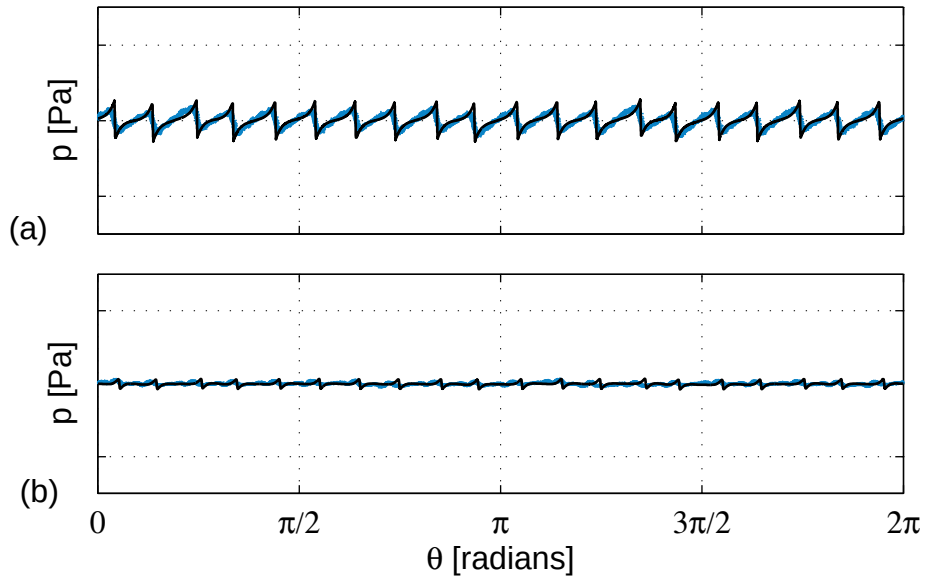

Fig. 19 Comparison between numerical results from the 1DNP-TFD code and measured data at (a) station 2 and (b) station 3. Sawtooth pressure waveform in the lined intake duct. Key: Black line—1DNP–TFD; Blue line—data.

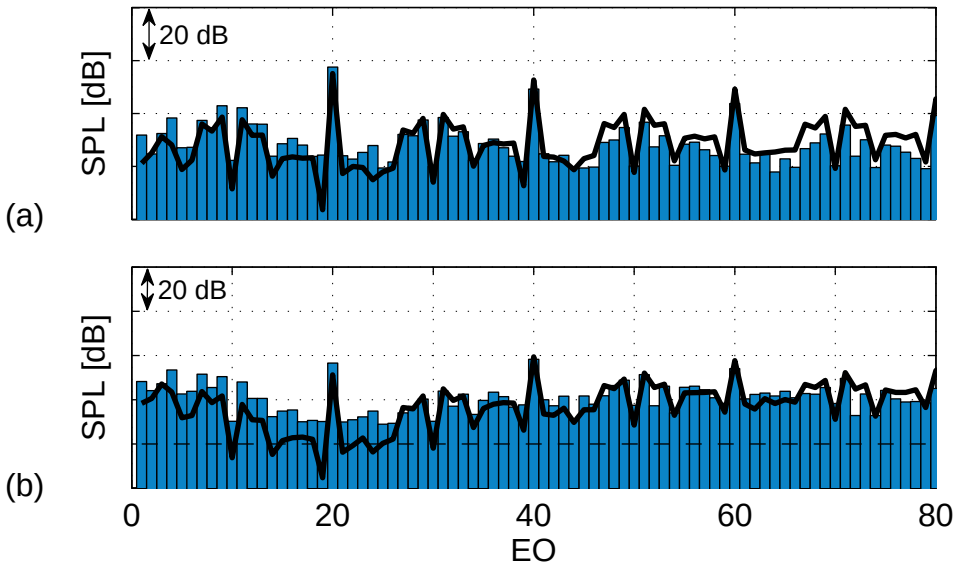

Fig. 20 Comparison between numerical results from the 1DNP-TFD code and measured data at (a) station 2 and (b) station 3. EO frequency spectrum in the lined intake duct. Key: Black line—1DNP–TFD; Blue bars—data.

the axial extent of the installed liner, and the locations where the results are compared, is shown in figure 16. Measurements were acquired close to the fan and within the region marked "axial microphone array". Comparisons are shown at axial stations 1 and 3 for the rigid intake, and stations 2 and 3 for the lined intake duct.

First the results from the 1DNP–TFD code and the measurements acquired in the rigid intake duct are compared. At the start of propagation, the comparison between measurement and prediction of the pressure waveform is shown in figure 17(a). This clearly shows that the irregular sawtooth closely represents the realistic waveform close to the fan. In the measured waveforms, the expansion waves are not exactly linear: they are slightly concave. The linear expansion waves used in the model do not capture this concave shape; it has been assumed that the expansion waves are linear from shock-to-shock. Another noticeable feature in the measurements is that the shocks are slightly spread out owing to the limit of the measurement sampling frequency used in data acquisition, but in the propagation model the shocks are represented by a finite jump from peak to trough.

Comparison between measurement and prediction of the EO frequency spectrum, shown in figure 18(a), only shows some small differences at the low-frequency tones, but otherwise the measured and predicted spectra are in very close agreement.

As the waveform is propagated to axial station 3 the comparison of the results shows that the attenuation of the shocks is reliably predicted, see figure 17(b). In the EO frequency spectrum, the predicted tone levels are similar to the measurements, especially at frequencies up to $2 \times$ BPF. Over this propagation distance, the shocks' amplitudes reduce to about 18 % of the initial shock amplitude at station 1, this corresponds to roughly a 20 dB reduction in the BPF tone.

Despite the fact that the curvature in the measured expansion waves is not represented in the sawtooth waveform prediction model, the predicted levels of the EO tones are in good agreement with the measured tone levels. The decay of the BPF tone and its harmonics, which are the dominant tones, is predicted by the numerical model, and all the features of the nonlinear propagation of the sawtooth waveform, such as shock amplitude decay, and shock position displacement, are successfully captured by the simulations.

Now compare the results from the 1DNP–TFD code and the measurements acquired in the lined intake duct. As shown illustrated in figure 16, the liner is installed from roughly $z/D = 0.1$ to 0.4, and stations 2 and 3 are situated within this lined section. Figures 19 and 20 show the sawtooth waveforms and spectral comparisons between the measurements and predictions, respectively. As noted in section II B 3, information about the double-layer lining used in the rig-scale fan test is proprietary, thus the liner decay rates used in the simulations by the 1DNP–TFD code are not shown. Measurements at station 1 were acquired in a rigid section before the installed acoustic liner, hence the measurements and predictions at this first station are very similar to the results for the rigid intake duct shown in figures 17(a) and 18(a).

At station 3, the sawtooth waveform is almost flat on the scale shown in figure 19(b), compared to the waveform at station 2. The shocks' locations in the predicted waveform closely match the measured waveform, albeit the expansion waves are slightly wavier. Prediction of the EO frequency spectrum, shown in figure 20, shows the direct effect of the acoustic liner absorption. The horizontal dashed line in figure 20(b) indicates the lower end of the vertical scale on figure 20(a), which shows that the tones are much more attenuated in the lined intake compared to the rigid intake duct. In fact, the BPF tone reduced by about 46 dB in the lined intake compared to about 20 dB in the rigid intake duct. In the spectral comparisons, the general shape of the measured tonal spectrum is well predicted. There is an over-prediction of the attenuation at the low frequencies, but minimal under-prediction of the attenuation at the higher frequencies. The over-prediction of the attenuation of the tones around blade passing frequency occurs within the liner's optimal frequency range. Clearly more liner absorption is predicted at these frequencies than occurs in practice.

V. Conclusion

A one-dimensional nonlinear propagation time-frequency domain model, referred to by the acronym 1DNP–TFD, has been developed and benchmarked against: (i) Analytic solutions for a regular sawtooth; (ii) Time-domain method for an irregular sawtooth propagating in a rigid cylindrical intake; (iii) Frequency-domain method for an irregular sawtooth propagating in a rigid and a lined cylindrical intake. The benchmark solutions (i)–(iii) are all nonlinear propagation methods which have been developed in previous work. The simulations calculate the nonlinear propagation of

a one-dimensional irregular sawtooth pressure waveform, which models the propagation of the rotor-locked pressure field generated when the aircraft engine fan blade tips relative speed is supersonic. There is excellent agreement observed between all the benchmark solutions and the time-frequency domain numerical method. The 1DNP–TFD code runs on a standard personal computer, and simulations based on the typical size of an aircraft engine's intake duct only take a few minutes to compute. Thus this method would be suitable to use for parametric and optimisation studies.

Brief validation results using rig-scale measured data shows that the predictions closely match the measured tone levels in the rigid intake duct. In the lined intake, the absorption of sound by the acoustic liner is modelled by transforming from the time to the frequency domain. Also, there is a reasonable level of agreement between the predictions and the measured tone levels in the lined intake duct.

The differences observed between measurement and prediction are presumably attributable to a number of real effects not implemented in the model. In the model, the intake is approximated by a cylindrical duct containing uniform flow. Of course, in reality the intake duct is not a cylinder, and the flow is non uniform. Additionally, boundary layers refract the upstream propagating sound away from the duct wall, which can affect the effective liner attenuation, see Refs. [11, 21, 27]. Some or all of these differences between the model and reality may account for the differences observed between measurement and prediction for supersonic fan "buzz-saw" tones produced in an aircraft engine's intake duct.

Finally, the time-frequency domain method provides a platform that can be developed to incorporate into the model more complex features of nonlinear propagation of supersonic fan tones. In particular the method is amenable to model an axisymmetric intake duct, whereby the duct's diameter and mean flow vary axially. The potential to develop the time-frequency domain method to use for simulations involving more complex models of the intake duct geometry and mean flow is the key reason for its development, since modelling the waveform's propagation in the time-domain and liner absorption in the frequency domain uses the preferred domain for each part of the modelling process. Also, coupling the propagation model to an appropriate radiation model in order to predict supersonic fan noise as it propagates from the fan to the far-field appears feasible.

All non-proprietary data supporting this study are openly available from the University of Southampton repository at http://dx.doi.org/10.5258/SOTON/xxxxx

Acknowledgments

The first author was supported via a Dorothy Hodgkin Postgraduate Award funded by the Engineering and Physical Science Research Council and Rolls–Royce plc. All the authors wish to acknowledge Rolls–Royce plc for the provision of the measured data shown in Section IV D, and their continuing financial support via the University Technology Centre in Gas Turbine Noise at the Institute of Sound and Vibration Research. Also this work has been reported on project "Whole Aircraft Multidisciplinary Noise Design System (HARMONY)" funded by Innovate UK, project reference number 101367.

[1] D. Casalino, F. Diozzi, R. Sannino, and A. Paonessa. Aircraft noise reduction technologies: A bibliographic review. *Aerospace Science and Technology*, 12(1):1–17, 2008 [doi: 10.1016/j.ast.2007.10.004].

[2] H.H. Hubbard. *Aeroacoustics of Flight Vehicles: Theory and Practice. Volume 1 - Noise Sources*. Woodbury: Published for the Acoustical Society of America through the American Institute of Physics, 1995.

[3] C.L. Morfey and M.J. Fisher. Shock-wave radiation from a supersonic ducted rotor. *The Aeronautical Journal of the Royal Aeronautical Society*, 74:579–585, 1970 [doi.org/10.1017/S0001924000049095].

[4] A. McAlpine and M.J. Fisher. On the prediction of buzz-saw noise in aero-engine inlet ducts. *Journal of Sound and Vibration*, 248(1):123–149, 2001 [dx.doi.org/10.1006/jsvi.2001.3770].

[5] Preliminary work on this method was presented at the 20th AIAA/CEAS Aeroacoustics conference, see reference [15].

[6] M.F. Hamilton and D.T. Blackstock, editors. *Nonlinear Acoustics*. Academic Press, 1998.

[7] M. Kassem. Validation of a one dimensional model for nonlinear propagation in air intake ducts. In *19th American Institute of Aeronautics and Astronautics AIAA/CEAS Aeroacoustics Conference, Berlin, Germany, May 27 - 29*, 2013 [dx.doi.org/10.2514/6.2013-2173].

[8] Dilip Prasad and Jinzhang Feng. Propagation and decay of shock waves in turbofan engine inlets. In *ASME Turbo Expo 2004: Power for Land, Sea, and Air*, pages 1733–1745. American Society of Mechanical Engineers, 2004 [doi:10.1115/GT2004-53949].

[9] J.S. Mendousse. Nonlinear dissipative distortion of progressive sound waves at moderate amplitudes. *The Journal of the Acoustical Society of America*, 25(1):51–54, 1953 [dx.doi.org/10.1121/1.1907007].

[10] I. Rudnick. On the attenuation of a repeated sawtooth shock wave. *The Journal of the Acoustical Society of America*, 25(5):1012–1013, 1953 [dx.doi.org/10.1121/1.1907197].

[11] A. McAlpine and M.J. Fisher. On the prediction of buzz-saw noise in acoustically lined aero-engine inlet ducts. *Journal of Sound and Vibration*, 265:175–200, 2003 [dx.doi.org/10.1016/S0022-460X(02)01446-3].

[12] A. McAlpine, M.J. Fisher, and B.J. Tester. Buzz-saw noise: A comparison of measurement with prediction. *Journal of sound and vibration*, 290(3):1202–1233, 2006.

[13] A. McAlpine, M.J. Fisher, and B.J. Tester. Buzz-saw noise: A comparison of modal measurements with an improved prediction method. *Journal of Sound and Vibration*, 306(3):419–443, 2007 [dx.doi.org/10.1016/j.jsv.2005.05.028].

[14] A. McAlpine, M.J.Fisher, B.J.Tester, and P.J.G.Schwaller. Buzz-saw noise: Prediction of the rotor-alone pressure field. *Journal of Sound and Vibration*, 331:4901–4918, 2012

[dx.doi.org/10.1016/j.jsv.2012.06.009].

[15] O.E. Adetifa, A. McAlpine, and G. Gabard. Modelling the nonlinear sound propagation and radiation of supersonic fan tones. *20th AIAA/CEAS Aeroacoutics conference, Atlanta USA*, AIAA 2014-2945, 2014 [dx.doi.org/10.2514/6.2014-2945].

[16] J. Thisse, C. Polacsek, S. Lewy, and A. Lafitte. On the generation and propagation of multiple pure tones inside turbofans at transonic regime. *20th AIAA/CEAS Aeroacoutics conference, Atlanta USA*, AIAA 2014-3104, 2014 [dx.doi.org/10.2514/6.2014-3104].

[17] Anil Prasad. Evolution of upstream propagating shock waves from a transonic compressor rotor. In *ASME Turbo Expo 2002: Power for Land, Sea, and Air*, pages 299–309. American Society of Mechanical Engineers, 2002 [doi:10.1115/GT2002-30356].

[18] F.M. Pestorius. Propagation of plane acoustic noise of finite amplitude. Technical Report ARL-TR-73-23 Applied Laboratories, The University of Texas at Austin AD778868, The University of Texas at Austin, 1973.

[19] M.J. Fisher, B.J. Tester, and P.J.G. Schwaller. Supersonic fan tone noise prediction. *American Institute of Aeronautics and Astronautics AIAA 34th Aeroacoustics Conference*, AIAA-98-2249:290–300, 1998 [dx.doi.org/10.2514/6.1998-2249].

[20] S. Uellenberg. Buzzsaw noise predictions for modern turbofans. *AIAA 2004-3000*, 2004 [dx.doi.org/10.2514/6.2004-3000]. Proceedings of the 10th AIAA/CEAS Aeroacoustics Conference, Manchester, UK, May 10–12, 9 pages.

[21] R. Sugimoto, R.J. Astley, and P.B. Murray. Low frequency liners for turbofan engines. In *Proceedings of the 20th International Congress on Acoustics*, 2010.

[22] R.E. Motsinger and R.E. Kraft. Design and performance of duct acoustic treatment. *In H.H. Hubbard (Ed.), Aeroacoustics of Flight Vehicles: Theory and Practice, Vol. 2, Noise Control, NASA RP-1258*, pages 165–206, 1991.

[23] Paul Murray and R. Jeremy Astley. Development of a single degree of freedom perforate impedance model under grazing flow and high SPL, AIAA 2012–2294. In *18th AIAA/CEAS Aeroacoustics Conference (33rd AIAA Aeroacoustics Conference)*, 2012 [dx.doi.org/10.2514/6.2012-2294].

[24] M.K. Myers. On the acoustic boundary condition in the presence of flow. *Journal of Sound and Vibration*, 71(3):429–434, 1980 [dx.doi.org/10.1016/0022-460X(80)90424-1].

[25] F.M. Pestorius, S.W. Williams, and D.T. Blackstock. Effect of nonlinearity on noise propagation. *Interagency Symposium on University Research on Transportation Noise*, June 1974.

[26] A. Korpel. Frequency approach to nonlinear dispersive waves. *Journal of Acoustic Society of America*, 67:1954–1958, 1980 [dx.doi.org/10.1121/1.384461].

[27] G. Gabard. A comparison of impedance boundary conditions for flow acoustics. *Journal of Sound and Vibration*, 332(4):714–724, 2013 [dx.doi.org/10.1016/j.jsv.2012.10.014].